CrossMark

ORIGINAL PAPER

The graphene/polypyrrole/chitosan-modified glassy carbon electrode for electrochemical nitrite detection

Qi Xiao[1] · Mengmeng Feng[1] · Yi Liu[1] · Shuangyan Lu[1] · Yingzi He[1] · Shan Huang[1]

Abstract A sensitive and selective electrochemical sensor based on carboxyl graphene (CG), polypyrrole (PPy), and chitosan (CS) nanocomposite-modified glassy carbon electrode (GCE) has been developed for nitrite determination. The electrochemical performances of CG/PPy/CS/GCE were characterized by cyclic voltammetry and electrochemical impedance spectroscopy. Under the optimum experimental conditions, CG/PPy/CS/GCE exhibited excellent differential pulse voltammetry (DPV) response of nitrite. A linear relationship between DPV peak current and the concentration of nitrite was obtained in the range of 0.2 to 1000 μM. The limit of detection of nitrite was estimated to be 0.02 μM. Using such modified electrodes, our method is quite reproducible for nitrite determination, even for real water samples.

Keywords Carboxyl graphene · Polypyrrole · Chitosan · Nitrite determination · Differential pulse voltammetry

Introduction

Nitrite anion (NO_2^-) is extensively used in food preservation and fertilizer industry. However, it is a toxic pollutant in soil, water, and physiological systems [1–3]. Nitrite concentration serves as an important indicator of organic pollution in water [4]. Excessive amount of nitrite anion in human blood will oxidize iron(II) in hemoglobin to form methemoglobin and inhibit oxygen transportation spontaneously, which causes the "blue baby syndrome" disease in infants [5]. Moreover, nitrite can also be converted to carcinogenic N-nitrosamines in the stomach, causing cancer and hypertension [6]. The limit of nitrite in meat products set by European Food Safety Authority is 50–100 mg nitrites per kg for some meat products [7]. The World Health Organization (WHO) has recommended the safe concentration of nitrite in drinking water of less than 3.0 mg L^{-1} [8, 9], and the US Environmental Protection Agency (EPA) has set the limit of nitrite in drinking water to be around 1.0 mg L^{-1} [10]. Thus, as a safety measure, the rapid extraction and low-level sensing of nitrite in environmental, biological, and food samples is a priority area of research. Up to date, a variety of techniques and various instrument-based methods have been developed to detect nitrite, such as spectrophotometry [5, 11], fluorescence spectrometry [12], chromatography [13], chemiluminescence [1, 14], and electrochemistry [2, 7, 8, 15]. Among these techniques, due to their easy operation, low operating cost, simultaneous determination, quick response, high sensitivity, and good stability, the electrochemical techniques have been widely applied for nitrite determination based on either oxidation or reduction of nitrite at different electrodes [16, 17]. However, few studies about nitrite oxidation have been reported owing to the relatively high overpotential [18]. Therefore, there is a bigger demand for the development of more reliable and efficient electrochemical sensor for sensitive analysis of nitrite with low detection limit.

Carboxyl graphene (CG), which is a single layer of carbon atoms and two-dimensional crystalline carbon material with carboxylic groups at the lateral edge, has currently attracted huge attention both in theoretical and practical research

✉ Shan Huang
huangs@whu.edu.cn

1 College of Chemistry and Materials Science, Guangxi Teachers Education University, Nanning 530001, People's Republic of China

owning to its excellent electric, thermal, chemical, and mechanical properties [19, 20]. In particular, CGs are negatively charged when dispersed in water due to the ionization of the carboxylic acid and phenolic hydroxyl groups, which results in that CG can form well-dispersed aqueous colloids ascribed to the electrostatic repulsion of these graphene sheets [21]. The specific structure CG makes has been proposed as a novel functional electrode material for developing electrochemical sensors for some important biomolecules with their carboxyl-containing functional groups [22, 23]. Liang and co-workers developed a direct electron transfer biosensor for determination of glucose based on glucose oxidase self-assembled on electrochemically reduced carboxyl graphene [22]. Huang et al. demonstrated an electrochemical sensor based on carboxylic acid functionalized graphene for simultaneous detection of adenine and guanine in DNA [23]. Such carboxyl functionalized graphene shows excellent electronic transport properties and high surface areas, so it is a good candidate for constructing electrochemical-based sensor. However, there are few reports indicating that CG has been used for nitrite sensor with direct electron transfer until now.

Accordingly, we fabricated an electrochemical sensor for highly sensitive and selective determination of nitrite by differential pulse voltammetry (DPV) analysis based on CG, polypyrrole (PPy), and chitosan (CS) nanocomposite-modified glassy carbon electrode (GCE) (Scheme 1). The combination of PPy and CG not only provides large surface area and numerous active sites but also improves the charge transfer between the electrode and the reagent [24]. Meanwhile, the abundant amino groups of CS make it attract negatively charged nitrite, which can effectively facilitate the accumulation of nitrite on the electrode surface [25]. Hence, it is possible to increase the selectivity and sensitivity for nitrite determination by using CG/PPy/CS nanocomposite through simple mixing CG, PPy, and CS. The fabricated CG/PPy/CS/GCE showed low detection limit, wide linear range, high specificity, and good stability. This CG/PPy/CS/GCE was successfully applied for nitrite determination in real water samples, and the recovery results showed good accuracy of the constructed CG/PPy/CS/GCE. This work demonstrates a promising path for developing a highly sensitive method to rapidly detect this important toxic anion.
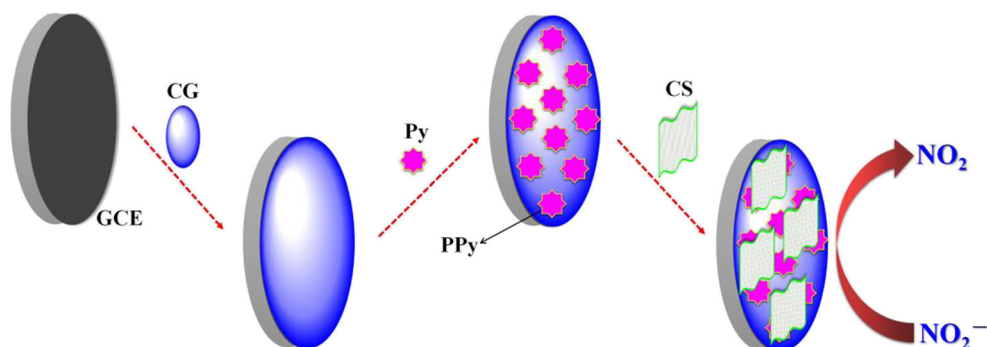
Materials and methods

Reagents and apparatus

CG was purchased from Nanjing XFNANO Materials Tech. Co. Ltd. (http://www.xfnano.com/). Pyrrole (Py) and CS were purchased from Aladdin (http://www.aladdin-e.com/us_en/). $NaNO_2$, KCl, $K_4[Fe(CN)_6]$, $K_3[Fe(CN)_6]$, Na_2CO_3, Na_2SO_4, $HgCl_2$, $MnCl_2$, $CuCl_2$, $MgCl_2$, $AlCl_3$, $CaCl_2$, $ZnCl_2$, $BaCl_2$, $CoCl_3$, $FeCl_3$, and $NaNO_3$ were all purchased from Sinopharm Chemical Reagent Factory (Shanghai, China). All reagents were of analytical grade and used as received without any further purification. Ultrapure water with a resistivity of 18.2 MΩ cm was produced by passing through a RiOs 8 unit followed by a Millipore-Q Academic purification set (Millipore, Bedford, MA, USA).

FT-IR spectra were recorded on a Nicolet iS10 spectrometer (Thermo, USA). Scanning electron microscopy (SEM) images were taken on MERLIN Compact field emission scanning electron microscope (ZEISS, Germany). Electrochemical experiments were performed on a CHI-660E electrochemical workstation (Shanghai Chenhua Instrument Co., Ltd., China) equipped with a thermostatic bath (DKB501S, Shanghai Jing Hong Laboratory Instrument Co. Ltd., China). A three-electrode cell was employed and GCE or modified GCE was used as working electrode. Ag/AgCl electrode served as the reference electrode and platinum wire was employed as the counter electrode. All pH measurements were made with basic pH meter PB-10 (Sartorius Scientific Instruments Co., Ltd., China).

Synthesis of PPy and CG/PPy nanocomposite

For PPy preparation, Py monomers were mixed with 0.1 M $FeCl_3$ solution. The mixture was centrifuged for several times until the pH of the filtrate was adjusted to around 7.0 by

Scheme 1 Fabrication process of CG/PPy/CS/GCE for sensitive detection of NO_2^-

adding 0.1 M NaOH solution or 0.1 M HCl solution. Then, the precipitate was dried at 60 °C for 12 h to remove the unpolymerized Py monomers. For CG/PPy nanocomposite preparation, CG and Py monomers were immersed in an ethanol solution for 1 h under continuous stirring. Then, 0.1 M FeCl$_3$ solution was added into the above suspension with continuous stirring for 1 h. After the polymerization of Py monomers on CG surface, the mixture was centrifuged for several times until the pH of the filtrate was adjusted to around 7.0 by adding 0.1 M NaOH solution or 0.1 M HCl solution. The precipitate was dried at 60 °C for 12 h to remove the unpolymerized Py monomers.

Preparation of CG/PPy/CS/GCE

Prior to modification, bare GCE was polished with 1.0, 0.3, and 0.05 μm alumina slurry subsequently on a polishing cloth; rinsed thoroughly with ultrapure water; and then sonicated in 0.5 M H$_2$SO$_4$, ethanol, and ultrapure water for 3 min. For the preparation of CG/PPy/CS/GCE, 4.0 mg CG/PPy nanocomposite was homogeneously dispersed in 1 mL 0.5 wt% CS solution at room temperature with the aid of ultrasonic agitation. Then, 4 μL of the homogenous suspension was dropped on the pretreated GCE surface by drop casting method and the modified electrode was dried under an infrared lamp for 20 min. The obtained CG/PPy/CS/GCE was rinsed with ultrapure water to remove the loose adsorbed materials. Alternatively, different kinds of modified electrodes such as CG/GCE, PPy/GCE, CG/PPy/GCE, and CG/CS/GCE were also fabricated with the above-mentioned similar procedure. The obtained modified electrodes were preserved in a refrigerator at 4 °C before applications.

Preparation of real water samples

For real water sample analysis, tap water, commercial Nongfu Spring water, salt water, and soybean milk samples were selected. The tap water was obtained from our lab. All water samples were purified by filtration with 0.22 μm Millipore filter three times to remove large solids and main impurities. The supernatant liquid of 500 μL was diluted to 1 mL with NaAc–HAc buffer (pH 4.0). After that, the solution was stored in dark at 4 °C. The solution was diluted 20-fold with NaAc–HAc buffer (pH 4.0) before analysis. Different amounts of nitrite standard solution were added into the reaction system. The final concentrations of nitrite were 5, 10, 20, 100, 200, and 500 μM, respectively. The recovery of nitrite in real water samples was examined by the method.

Procedures for nitrite determination

DPV responses of CG/PPy/CS/GCE to different concentrations of sodium nitrite in NaAc–HAc buffer (pH 4.0) were carefully investigated with instrumental parameters as potentials range from 0.4 to 1.2 V; pulse amplitude 0.05 V; pulse width 0.05 s; sampling width 0.0167 s; pulse period 0.5 s; quiet time 2 s; scan rate 0.05 V s^{-1}. Cyclic voltammetry (CV) measurements and electrochemical impedance spectrometry (EIS) experiments were carried out in 5.0 mM [Fe(CN)$_6$]$^{3-/4-}$ solution containing 0.1 M KCl.

Results and discussion

Choice of CG/PPy/CS nanocomposite

CG possesses abundant negatively charged functional groups and high surface areas, so it is a good candidate for constructing electrochemical sensors for different important biomolecules [22, 23]. Different kinds of graphene nanomaterials including CG can be used to modify GCE through the strong π–π stacking interaction. PPy, which is one of the most important conducting polymers, has been utilized extensively in electrochemical assays [24]. Due to its strong adhesion ability and the similar sp^2 bond character with carbons, PPy can be adsorbed on CG surface to form PPy layers [26]. FT-IR spectrometry can be used to investigate the interaction between CG and PPy. As shown in Fig. 1a, CG exhibits a very weak intensity and fairly broad band of O–H group from 3000 to 3750 cm^{-1}. This is ascribed to the adsorbed water molecules and the residual carboxylic acid and phenolic hydroxyl functionalities on CG surface. The absorption peaks at 1731 and 1614 cm^{-1} are assigned to the stretching vibration of C=O group and the bending vibration of C=C group, respectively [27, 28]. Meanwhile, the typical vibrations of Py are clearly observed at 1467 and 1547 cm^{-1} both in PPy and CG/PPy, suggesting the symmetric and the antisymmetric ring stretching of PPy [25]. The absorption peaks at 1180 and 1044 cm^{-1} in PPy are due to the plane vibrations of C–H in the Py ring. It is noteworthy that the characterized absorption peaks of PPy at 1467 and 1547 cm^{-1} are shifted to 1474 and 1551 cm^{-1} at CG/PPy nanocomposite, and the stretching vibration of C=O group at 1731 cm^{-1} of CG is shifted to 1728 cm^{-1} in CG/PPy nanocomposite, respectively, which is ascribed to the strong π–π stacking interaction between CG and PPy. Such interaction during CG/PPy nanocomposite leads to the broader absorption in high wavenumber range from 3000 to 3750 cm^{-1}, suggesting the formation of hydrogen bonds between CG and PPy.

CS is a class of linear hydrophilic polysaccharide obtained by deacetylation of nature chitin. Since CS is an attractive biocompatible and nontoxic natural biopolymer, it has been widely used as the immobilization matrix in bioelectrochemical processes [29]. Due to its relatively weak conductivity and desirable properties, CS is usually combined with conductive nanomaterials, such as graphene and carbon nanotubes [25, 30], to construct electrochemical sensing platforms. The

constructed CG/PPy/CS nanocomposite has excellent conductivity for enhancing the charge transfer and a large surface area for providing several active sites, which can increase the peak currents of the modified electrode. Meanwhile, CS has abundant primary amino and hydroxyl groups in the structure; the abundant functional groups of CS can effectively enhance the proton conductivity and attract negatively charged ions such as NO_2^- [25, 30], resulting in the accumulation of nitrite ions on the electrode surface. Therefore, CS is utilized to not only enhance the conductivity of bulk-quantity CG/PPy nanocomposite but also facilitate the accumulation of NO_2^-, which increase the sensitivity for NO_2^- determination tremendously.

Characterization of CG/PPy/CS/GCE

The microscopy technique is generally used to characterize the surface modification of the electrode [25]. SEM images of CG/GCE, CG/PPy/GCE, and CG/PPy/CS/GCE were recorded and illustrated in Fig. 2. As can be seen in Fig. 2a, a sheet-like CG is formed on the surface of GCE with a crimple effect. From Fig. 2b, the surface of CG is covered with fine granules of PPy, indicating that CG is well coated with PPy. However, the distribution of PPy in CG sheets is irregular, ascribed to the insulating feature of CG and the random binding ability of PPy on CG sheets. This situation can be efficiently improved in CG/PPy/CS/GCE, since a compact and homogeneous CG/PPy/CS film is formed on GCE surface (Fig. 2c). The formation of CG/PPy/CS nanocomposite not only maintains the strong binding ability of PPy on CG sheets but also efficiently enhances the dispersive capacity of PPy. Therefore, a compact and homogeneous CG/PPy/CS film is established on GCE surface. From the SEM image of CG/PPy/CS at lower magnification (Fig. 2d), compact and uniform fine granules can be observed, suggesting that CG/PPy/CS film is well dispersed on GCE surface.

CV is a valid technique to obtain the surface information about the modified electrodes [31, 32]. As evidenced in Fig.

1b, the CV signals of 5.0 mM $[Fe(CN)_6]^{3-/4-}$ redox couple (1:1) at bare GCE and different substance-modified GCE have been examined in 0.1 M KCl solution. It is obvious that both the anodic and cathodic peak currents of $[Fe(CN)_6]^{3-/4-}$ redox couple at CG/GCE are much lower than those of $[Fe(CN)_6]^{3-/4-}$ redox couple at bare GCE. Since the negatively charged CG can form well-dispersed aqueous colloids on GCE surface [21], the electron transfer ability between $[Fe(CN)_6]^{3-/4-}$ redox couple and electrode surface is reduced significantly. However, this situation can be improved efficiently after the addition of PPy. Since PPy can combine with CG through the strong π–π stacking interaction, the charge transfer between $[Fe(CN)_6]^{3-/4-}$ redox couple and electrode surface can be efficiently improved at CG/PPy/GCE. As further evidenced in Fig. 1b, the surface modification of PPy can increase the anodic and cathodic peak currents slightly, proving the better conductivity of PPy than that of CG. Therefore, the combination of CG and PPy can improve the conductivity of the electrode significantly. On the other hand, after the addition of CS into CG/PPy nanocomposite, the stability of CG/PPy/CS/GCE increases dramatically, and both the anodic and cathodic peak currents of $[Fe(CN)_6]^{3-/4-}$ redox couple at CG/PPy/CS/GCE increase dramatically than those of $[Fe(CN)_6]^{3-/4-}$ redox couple at CG/PPy/GCE (Fig. 1b), proving the good electron conductivity of $[Fe(CN)_6]^{3-/4-}$ redox couple at CG/PPy/CS/GCE.

EIS is further used to study the change of the interfacial property of electrodes and provide information on the impedance variations of electrode surface/electrolyte solution [33, 34]. Figure 1c shows the typical Nyquist plots of $[Fe(CN)_6]^{3-/4-}$ redox couple at bare GCE and different substances modified GCE in 0.1 M KCl solution with the frequencies swept from 10^4 to 0.1 Hz. For common species, the typical EIS curve includes a linear part and a semicircular part. Herein, the linear part at lower frequencies suggests the diffusion-limited process while the semicircular portion at higher frequencies implies the electron transfer-limited process. The diameter of the semicircular portion, which reflects the electron transfer
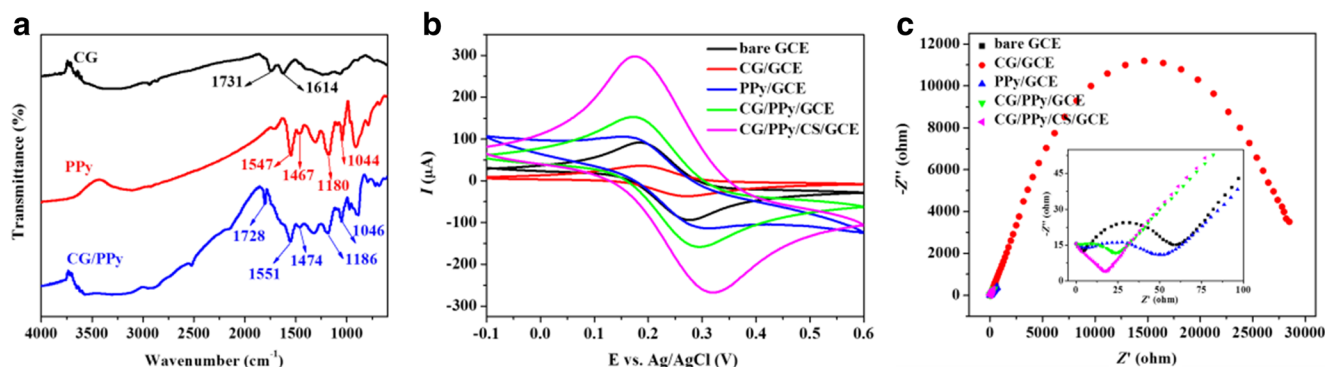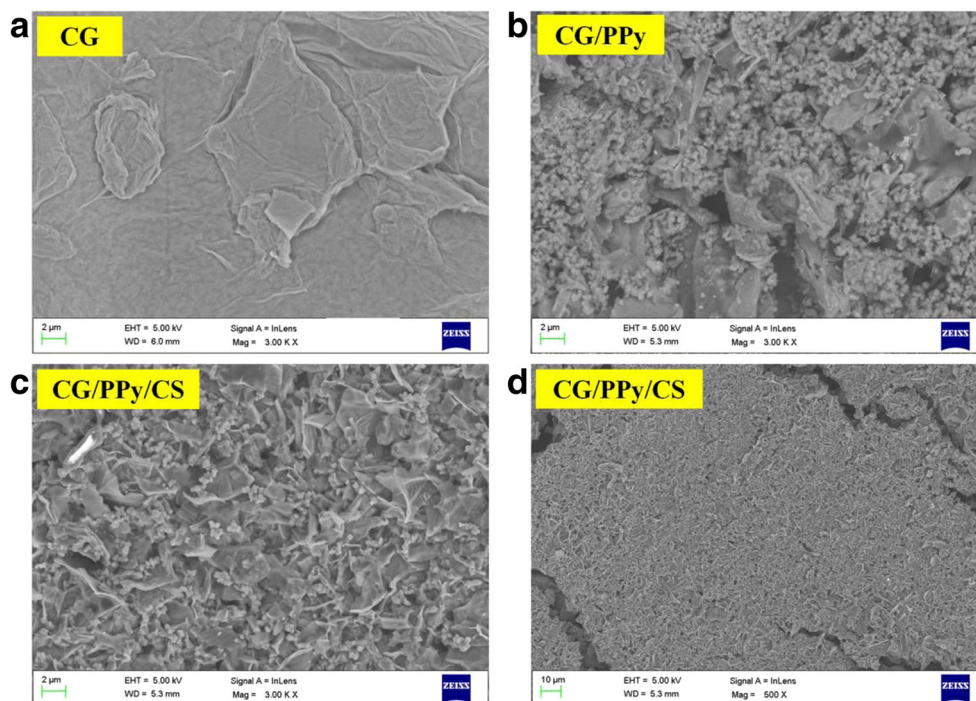

Fig. 1 **a** FT-IR spectra of CG, PPy, and CG/PPy. **b** CVs response of 5.0 mM $[Fe(CN)_6]^{3-/4-}$ redox couple (1:1) at bare GCE, CG/GCE, PPy/GCE, CG/PPy/GCE, and CG/PPy/CS/GCE in 0.1 M KCl solution with sweep rate of 50 mV s^{-1}. **c** Nyquist plots of 5.0 mM $[Fe(CN)_6]^{3-/4-}$ redox couple (1:1) at bare GCE, CG/GCE, PPy/GCE, CG/PPy/GCE, and CG/PPy/CS/GCE in 0.1 M KCl solution with the frequencies swept from 10^4 to 0.1 Hz

resistance R_{ct}, refers to the electron transfer kinetics of the redox probe at the electrode surface. As shown in Fig. 1c, CG/GCE shows the biggest diameter of the semicircular part than bare GCE, indicating the highest electron transfer resistance at CG/GCE. Other three modified electrodes exhibit much smaller diameter of the semicircular part than bare GCE, implying that the modifications of PPy, CG/PPy nanocomposite, and CG/PPy/CS nanocomposite on the surface of GCE can efficiently promote the electron transfer between $[Fe(CN)_6]^{3-/4-}$ redox couple and electrode interface. These results agreed well with the results obtained by CV (Fig. 1b).

Meanwhile, the CG/PPy/GCE exhibits smaller R_{ct} than bare GCE and PPy/GCE, suggesting that CG/PPy nanocomposite is an excellent electric-conducting material to accelerate the electron transfer on electrode surface. After the surface modification of CG/PPy/CS nanocomposite, a significant decrease in R_{ct} is observed due to the higher stability of CG/PPy/CS nanocomposite and the facilitated electron transfer of CG/PPy/CS nanocomposite. These results indicate that the electron transfer rate between $[Fe(CN)_6]^{3-/4-}$ redox couple and electrode surface is very slow on CG/GCE. However, the presence of CG/PPy nanocomposite and CG/PPy/CS nanocomposite
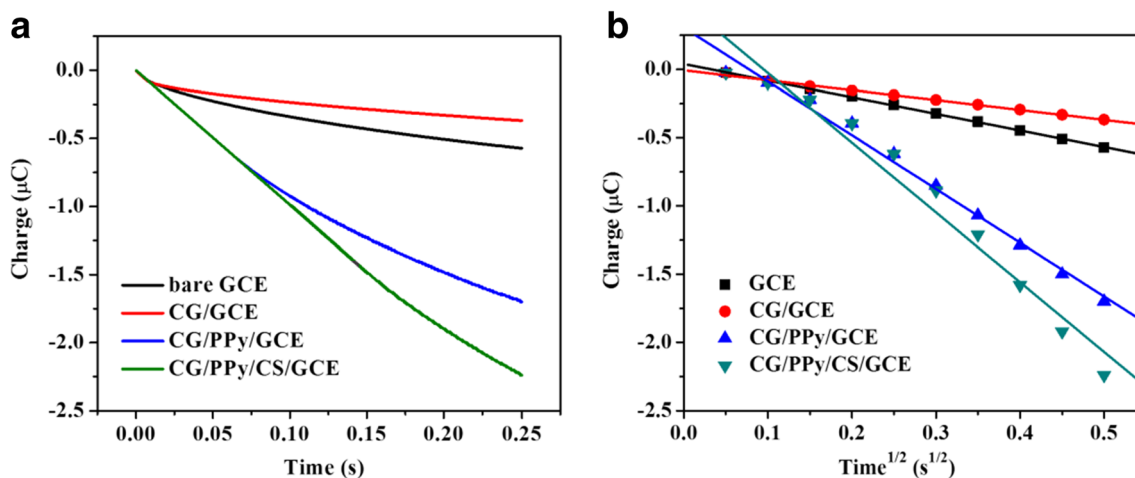

Fig. 3 Plots of $Q - t$ (a) and $Q - t^{1/2}$ (b) curves of 0.1 mM $K_3Fe(CN)_6$ at bare GCE, CG/GCE, CG/PPy/GCE, and CG/PPy/CS/GCE in 0.1 M KCl solution with the potentials swept from 0.15 to 0.25 V

can effectively improve the conductivity of the electrode and significantly facilitate the electron transfer between $[Fe(CN)_6]^{3-/4-}$ redox couple and electrode surface.

Chronocoulometry is further used to calculate the effective surface areas (A) of bare GCE and different substances modified electrodes. $K_3Fe(CN)_6$ with concentration of 0.1 mM is choosing as the model complex during chronocoulometry, and the diffusion coefficient (D) of $K_3Fe(CN)_6$ is reported to be about 7.63×10^{-6} cm^2 s^{-1} [35, 36]. The effective surface area of the working electrode can be calculated through the following equation [37]:

$$Q(t) = \frac{2nFAcD^{1/2}t^{1/2}}{\pi^{1/2}} + Q_{dl} + Q_{ads} \tag{1}$$

Herein, $Q(t)$ represents the electron transfer charge at the specific time t, n is the electron transfer number, F is the Faraday's constant, and c is the concentration of the substrate, respectively. Q_{dl} and Q_{ads} represent the double-layer charge and the Faradic charge, respectively. Therefore, the A value can be calculated from the slope of the $Q - t^{1/2}$ curve. Figure 3 exhibits the plots of $Q - t$ and $Q - t^{1/2}$ curves of bare GCE, CG/GCE, CG/PPy/GCE, and CG/PPy/CS/GCE in 0.1 mM $K_3Fe(CN)_6$ solution containing 0.1 M KCl with the potentials swept from 0.15 to 0.25 V. The calculated effective surface area of CG/PPy/CS/GCE is 0.170 cm^2, which is much higher than the effective surface areas of bare GCE (0.041 cm^2), CG/GCE (0.025 cm^2), and CG/PPy/GCE (0.131 cm^2). Relative high effective surface area of CG/PPy/CS/GCE may enhance the peak current response signal, which is favorable for the construction of highly sensitive electrochemical sensing platform for NO_2^-.

During the quasi-reversible reaction, the electron transfer rate is comparable with diffusion rate and the peak potential separation (ΔE_p) increases with the increase of the sweep rate (v). In particular, when the ΔE_p values are higher than 65 mV above a certain sweep rate, the expected value for a one-electron transfer reaction has a purely Nernstian behavior. Thus, the standard electrochemical rate constant (k^{Θ}) value can be determined according to the Nicholson's methods [38, 39]:

$$\psi = k^{\Theta} \left(\frac{D_O}{D_R}\right)^{\alpha/2} \sqrt{\frac{RT}{\pi nFD_O v}} \tag{2}$$

$$\psi = \frac{-0.6288 + 0.0021n\Delta E_P}{1 - 0.017n\Delta E_P} \tag{3}$$

where ψ is the dimensionless kinetic parameter determined from ΔE_p and α is the charge transfer coefficient, respectively. D_O and D_R are the diffusion coefficients of the oxidized form $K_3Fe(CN)_6$ and the reduced form $K_4Fe(CN)_6$, respectively. F is the Faraday constant, and R and T have their usual meanings. The widely accepted values of D_O for $K_3Fe(CN)_6$ and

D_R for $K_4Fe(CN)_6$ are 7.63×10^{-6} and 6.32×10^{-6} cm^2 s^{-1}, respectively [36]. In most cases, the reduction and oxidation kinetics are fairly symmetrical and the value of α is set as 0.5 [40]. Therefore, the k^{Θ} value depends solely on the value of ψ (one-electron processes).

According to the above equations, the k^{Θ} value can be calculated from the slope of the $\psi - v^{-0.5}$ curve. Figure 4 shows the CV curves and associated kinetic analyses of $[Fe(CN)_6]^{3-/4-}$ redox couple at bare GCE and different substance-modified electrodes. As shown in Fig. 4, $[Fe(CN)_6]^{3-/4-}$ redox couple at bare GCE and three modified electrodes all exhibit the characteristics of quasi-reversibility with sweep rates increasing from 50 to 300 mV s^{-1}. The calculated average k^{Θ} values of $[Fe(CN)_6]^{3-/4-}$ redox couple at bare GCE, CG/GCE, CG/PPy/GCE, and CG/PPy/CS/GCE are about 5.29×10^{-3}, 7.15×10^{-3}, 2.26×10^{-3}, and 1.88×10^{-3} cm s^{-1}, respectively. The k^{Θ} value of $[Fe(CN)_6]^{3-/4-}$ redox couple at CG/PPy/CS/GCE is therefore the lowest among those of $[Fe(CN)_6]^{3-/4-}$ redox couple at bare GCE and other substance-modified GCE, implying the slower electron transfer kinetic for CG/PPy/CS/GCE.

The electron transfer ability of electrode is closely related with the surface coverage of the electrode [41]. In summary, the electron transfer ability of $[Fe(CN)_6]^{3-/4-}$ redox couple may increase as the surface coverage increases until a critical surface coverage and the further increase in surface coverage can result in the decrease of $[Fe(CN)_6]^{3-/4-}$ redox couple diffusion coefficient. As shown in Fig. 5, the k^{Θ} value of $[Fe(CN)_6]^{3-/4-}$ redox couple at CG/GCE increases as the concentration of CG increases from 1 to 3 mg mL^{-1} and then decreases when the concentration of CG is higher than 3 mg mL^{-1}. Herein, 4 mg mL^{-1} CG is used for construct CG/PPy/CS/GCE, so the surface coverage is more than the critical surface coverage and the k^{Θ} value of $[Fe(CN)_6]^{3-/4-}$ redox couple at CG/PPy/CS/GCE is naturally lower than the maximum k^{Θ} value.

Electrochemical response of CG/PPy/CS/GCE to nitrite

The electrochemical response of CG/PPy/CS/GCE to NO_2^- can be demonstrated from DPV responses of 1 mM NO_2^- in 0.1 M NaAc–HAc buffer (pH 4.0). As shown in Fig. 6a, NO_2^- shows a tiny DPV oxidation peak current of − 4.47 μA at peak potential of 0.904 V at bare GCE, and NO_2^- also shows tiny DPV oxidation peak current of − 3.96 μA at peak potential of 0.828 V at CG/GCE, which are regarded as the blank responses. On the other hand, NO_2^- exhibits relatively higher DPV oxidation peak current of − 7.43 μA at peak potential of 0.952 V at PPy/GCE. Furthermore, the addition of CG can affect the DPV response of NO_2^- at PPy/GCE to some extent. After the successful modification of CG/PPy on the surface of same GCE, the oxidation peak current of NO_2^- is increased to
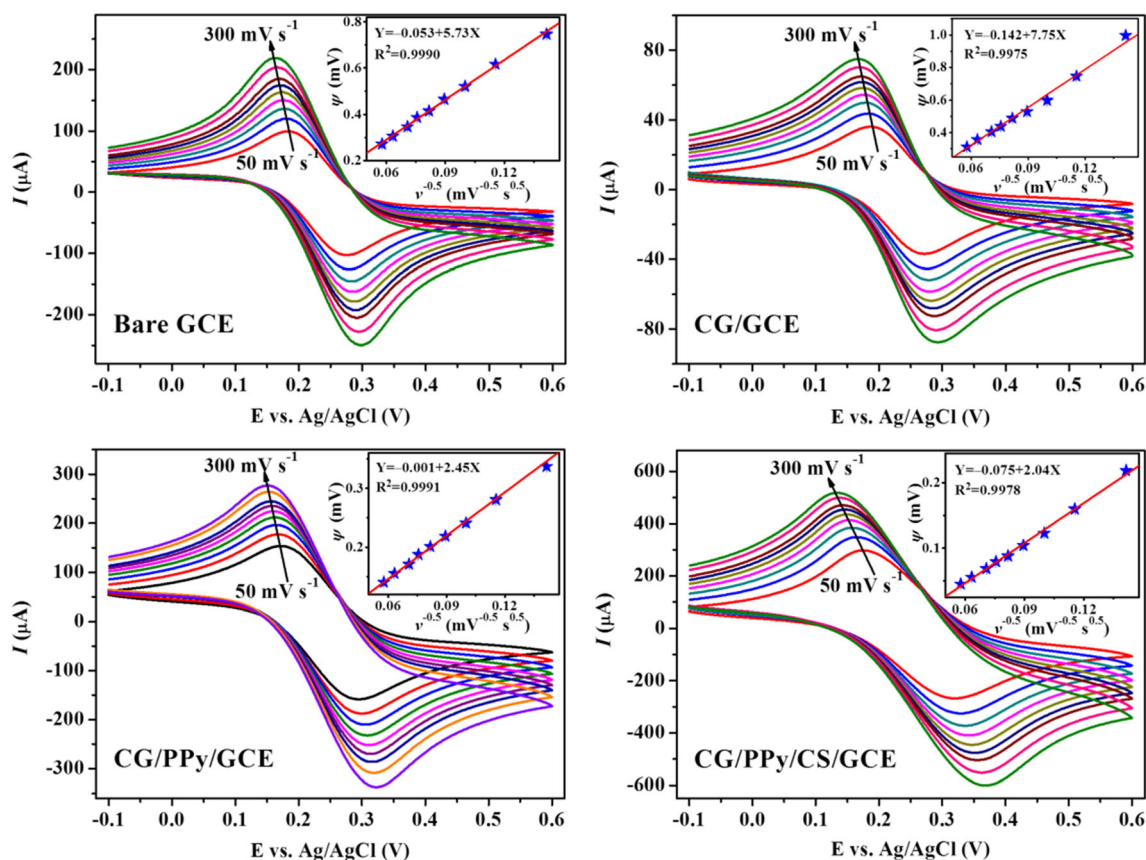
Fig. 4 CVs and associated kinetic analyses of 5.0 mM $[Fe(CN)_6]^{3-/4-}$ redox couple (1:1) at bare GCE, CG/GCE, CG/PPy/GCE, and CG/PPy/CS/GCE in 0.1 M KCl solution. Inserts were the corresponding plots of $\psi - v^{-0.5}$ curves. Sweep rates 50, 75, 100, 125, 150, 175, 200, 250, and 300 mV s^{-1}

− 8.43 μA at peak potential of 0.912 V. Most importantly, further addition of CS on CG/PPy/GCE causes a significant increase in the DPV response. The oxidation peak current of NO_2^- on CG/PPy/CS/GCE is observed to be − 12.7 μA at peak potential of 0.876 V. The DPV peak current of NO_2^- at CG/PPy/CS/GCE is obviously larger than those of NO_2^- at bare GCE and other modified electrodes. The oxidation peak potential is observed in the less positive side (i.e., 0.912 V at CG/PPy/GCE to 0.876 V at CG/PPy/CS/GCE), and the oxidation peak current increases by 1.5 times (i.e., − 8.43 μA at CG/PPy/GCE to − 12.7 μA at CG/PPy/CS/GCE), which validates the enhancement of the electron transfer ability of NO_2^- on the surface of CG/PPy/CS/GCE. Compared with bare GCE, CG/GCE, PPy/GCE, and CG/PPy/GCE, CG/PPy/CS/GCE presents extra sharper peak current. In addition, due to the better absorbability and the higher conductivity of CG/PPy/CS nanocomposite toward target nitrite anion, the peak current difference of NO_2^- at CG/PPy/CS/GCE is much higher than those of NO_2^- at bare GCE and other modified electrodes (Fig. 6b), indicating that the developed CG/PPy/CS/GCE can be a promising excellent electrochemical sensing platform for NO_2^- determination.

Electrochemical reaction of NO_2^- may be dependent on the diffusion and/or adsorption of NO_2^- to electrode surface, which can be elucidated by the relationship between the oxidation peak current and scan rate [42]. If the electrochemical reaction is controlled by the adsorption process, the oxidation peak current is linear to the scan rate; when the electrochemical reaction is controlled by the diffusion process, the oxidation peak current is linear to the square root of the scan rate [43]. As shown in Fig. 7a, the oxidation peak current of NO_2^- at CG/PPy/CS/GCE increases gradually and the oxidation peak potential of NO_2^- at CG/PPy/CS/GCE shifts more positive value with the scan rate increasing from 25 to 300 mV s^{-1}, implying the typical irreversible electrochemical reaction [44]. As indicated in Fig. 7b, the oxidation peak current of NO_2^- is directly proportional to the scan rate, and the regression equation is I_{pa} (μA) = − 0.1517 v (mV s^{-1}) − 18.0043 with correlation coefficient of 0.9977. Furthermore, the oxidation peak current of NO_2^- is also directly proportional to the square root of the scan rate, and the regression equation is I_{pa} (μA) = − 3.3485 $v^{0.5}$ (mV s^{-1})$^{0.5}$ − 4.7268 with correlation coefficient of 0.9996 (Fig. 7c). These results suggest that the electrochemical oxidation of NO_2^- on CG/PPy/CS/GCE surface may be controlled by not only the adsorption process but also the diffusion process.

For the adsorption-controlled irreversible electrochemical reaction, the relationship between E_{pa} and v is described by the following equation [45]:

$$E_{pa} = E^{\Theta} + \left(\frac{RT}{\alpha nF}\right)\ln\left(\frac{RTk^{\Theta}}{\alpha nF}\right) + \left(\frac{RT}{\alpha nF}\right)\ln v \quad (4)$$

Herein, R, T, and F have their usual meanings, respectively. E^{Θ} is the formal redox potential, k^{Θ} is the standard rate constant of electrochemical reaction, α represents the electron transfer coefficient, and n means the electron transfer number, respectively. As shown in Fig. 7d, the oxidation peak potential of NO_2^- at CG/PPy/CS/GCE is directly proportional to the natural logarithm of the scan rate. The fitted regression equation is E_{pa} (V) = 0.04305 ln v (mV s^{-1}) + 0.8344 with correlation coefficient of 0.9968. Therefore, the value of αn was calculated to be around 0.6. Since the value of α is usually in the range of 0.3 to 0.7 in absolutely irreversible electrode
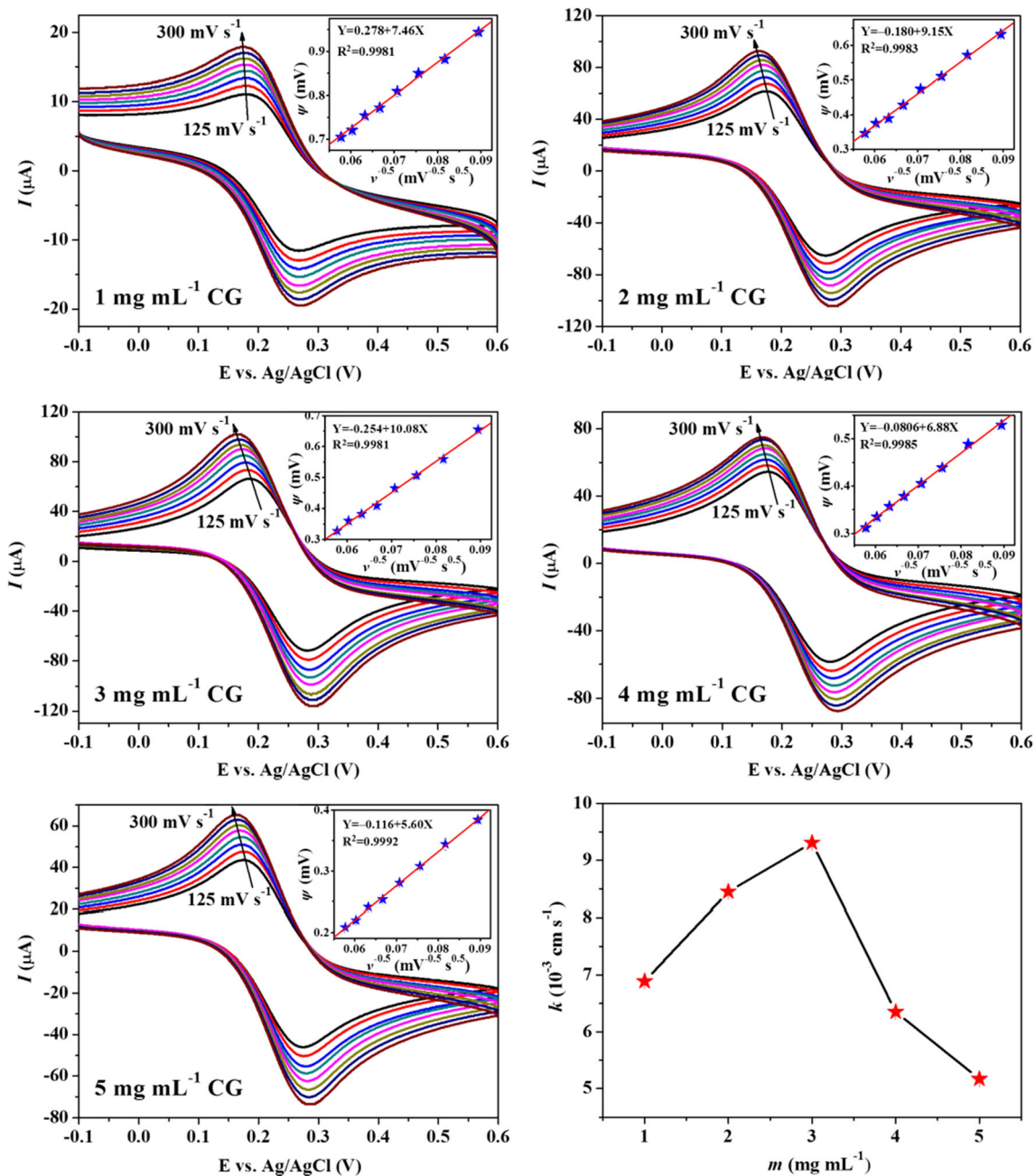

Fig. 5 CVs and associated kinetic analyses of 5.0 mM [Fe(CN)$_6$]$^{3-/4-}$ redox couple (1:1) at CG/GCE in 0.1 M KCl solution with different amounts of CG, and the plot of rate constant versus the amount of CG. Inserts were the corresponding plots of $\psi - v^{-0.5}$ curves. Sweep rates 125, 150, 175, 200, 225, 250, 275, and 300 mV s^{-1}
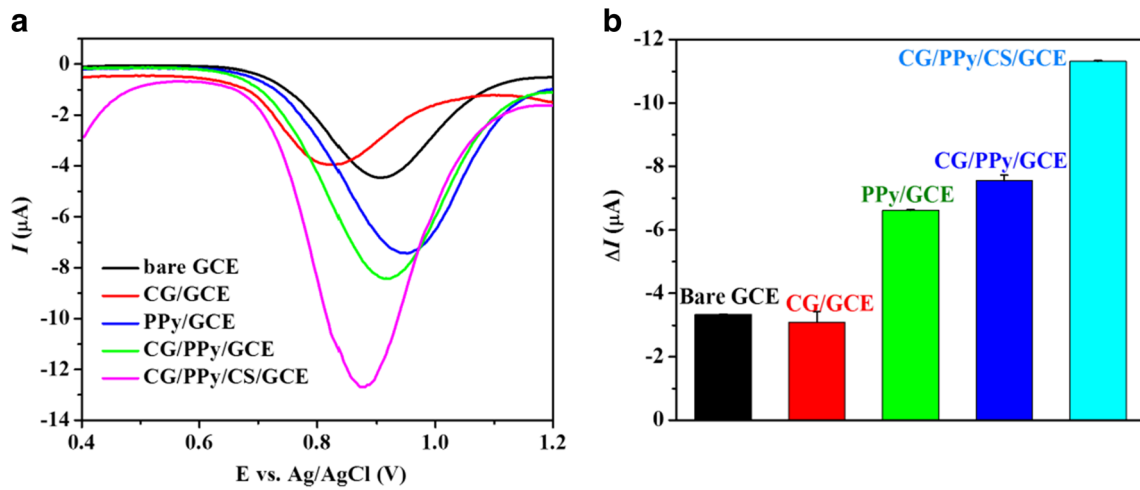
Fig. 6 **a** DPV curves of 1 mM NO_2^- at bare GCE, CG/GCE, CG/PPy/GCE, and CG/PPy/CS/GCE in 0.1 M NaAc–HAc buffer (pH 4.0). **b** DPV peak current differences of 1 mM NO_2^- at bare GCE, CG/GCE, CG/PPy/GCE, and CG/PPy/CS/GCE in 0.1 M NaAc–HAc buffer (pH 4.0)

process [46], it is speculated that the values of α and n are 0.6 and 1, respectively. Thus, the electrochemical oxidation process of NO_2^- at CG/PPy/CS/GCE surface is confirmed to be a one-electron transfer process [47].

The electrochemical catalyst of CG/PPy/CS nanocomposite for the oxidation of NO_2^- can be demonstrated from DPV responses in 0.1 M NaAc–HAc buffer (pH 4.0) at different temperatures using controlled thermostatic bath, and the results
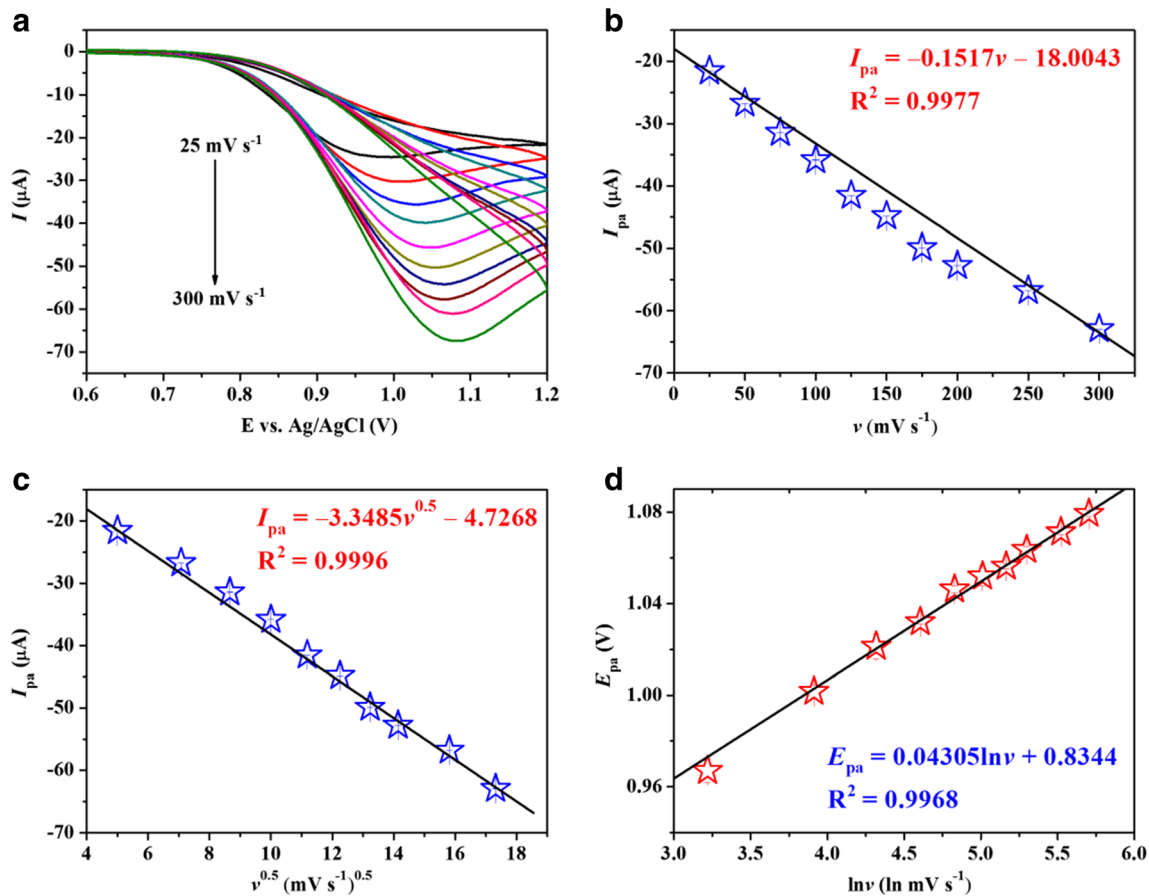

Fig. 7 **a** CVs of 1.0 mM NO_2^- at CG/PPy/CS/GCE with different scan rates. Curves were obtained at 25, 50, 75, 100, 125, 150, 200, 250, and 300 mV s^{-1}, respectively. **b** Plot of DPV peak current of 1.0 mM NO_2^- versus scan rate. **c** Plot of DPV peak current of 1.0 mM NO_2^- versus the square root of scan rate. **d** Plot of DPV peak potential of 1.0 mM NO_2^- versus the natural logarithm of scan rate
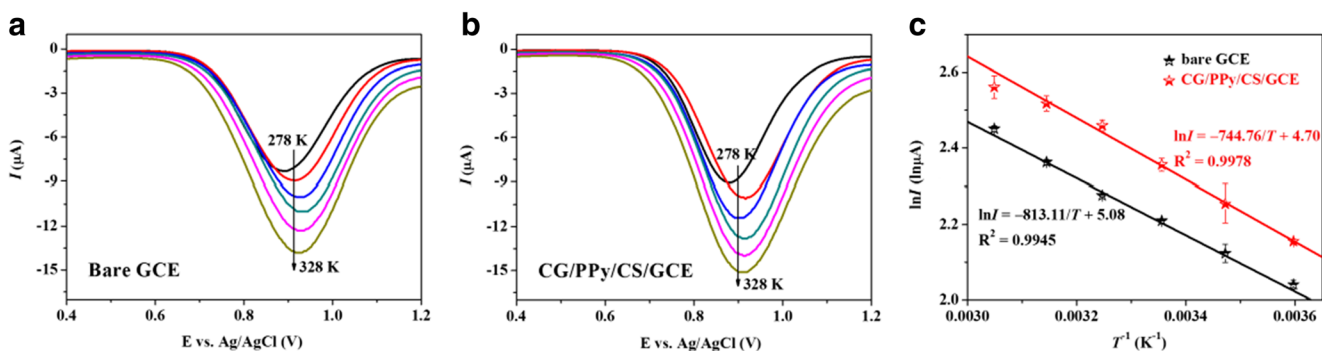
Fig. 8 **a** DPV responses of 1 mM NO_2^- at bare GCE in 0.1 M NaAc–HAc buffer (pH 4.0) under several different temperatures. **b** DPV responses of 1 mM NO_2^- at CG/PPy/CS/GCE in 0.1 M NaAc–HAc buffer (pH 4.0) under several different temperatures. **c** Plots of ln I versus T^{-1} for 1 mM NO_2^- at bare GCE and CG/PPy/CS/GCE. Results were expressed as the average of three independent experiments. Error bars represent standard deviations

are shown in Fig. 8a, b. The relationships between the natural logarithm of peak currents and the reciprocal of temperature are further displayed in Fig. 8c. It is obvious that the peak currents of NO_2^- on CG/PPy/CS/GCE are all larger than those of NO_2^- on bare GCE during all the measuring temperatures, which

suggests ulteriorly that CG/PPy/CS nanocomposite has better electrocatalytic performance. The oxidation peak potential tends to be negative, suggesting that the oxidation of NO_2^- is preferred at higher temperature. Additionally, the relationship between the catalytic rate constant (k) and the apparent
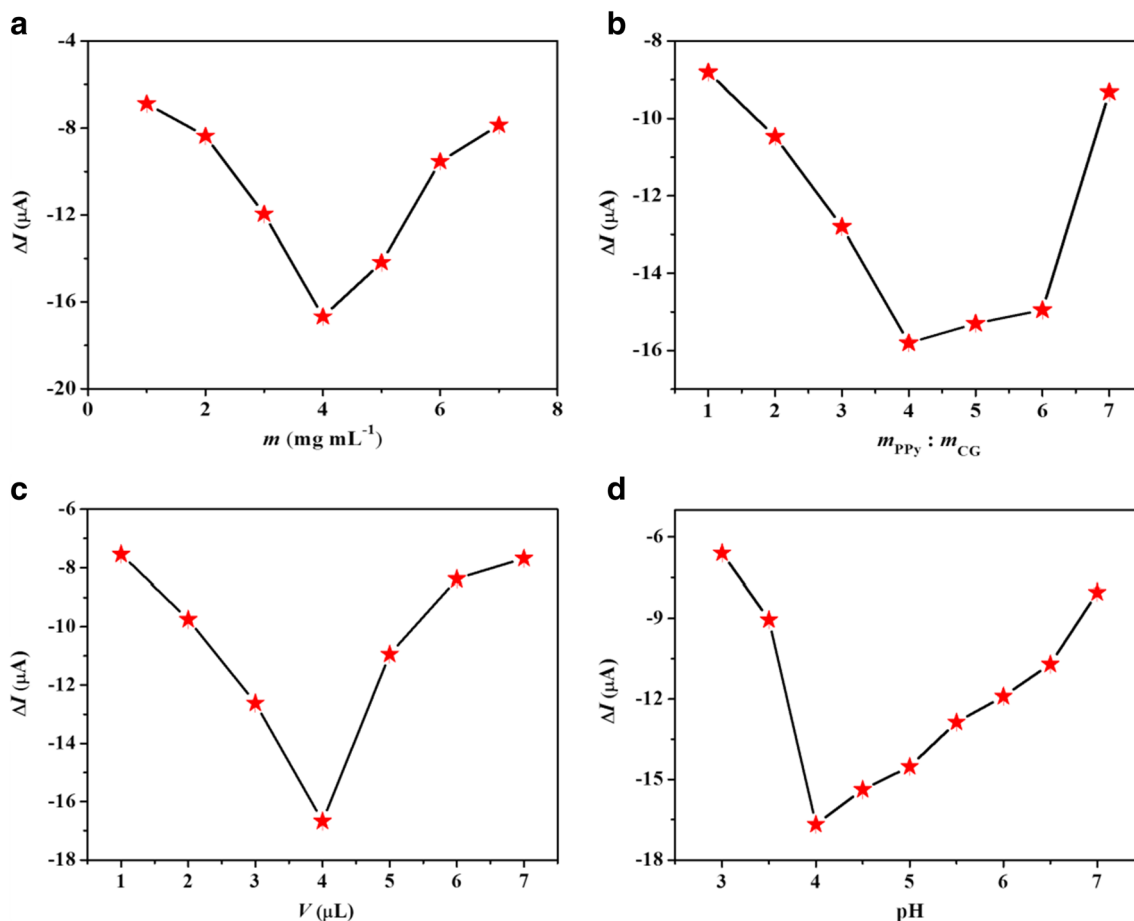

Fig. 9 Influence of **a** CG amount, **b** amount ratio of Py to CG, **c** addition volume, **d** buffer pH value on the DPV responses of 1 mM NO_2^- at CG/PPy/CS/GCE in 0.1 M NaAc–HAc buffer (pH 4.0). Results were expressed as the average of three independent experiments. Error bars represent standard deviations
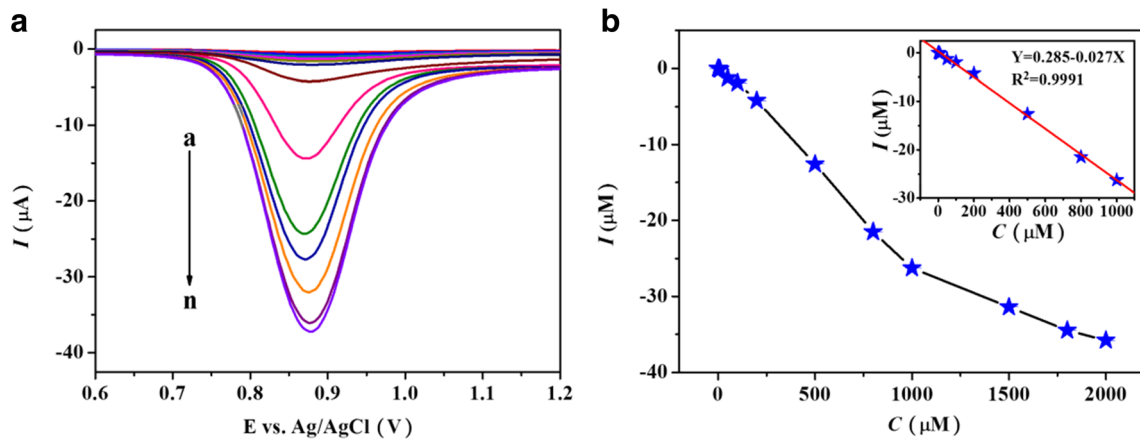
Fig. 10 **a** DPV responses of CG/PPy/CS/GCE to NO_2^- at concentrations of 0 (a), 0.2 (b), 1 (c), 5 (d), 10 (e), 50 (f), 100 (g), 200 (h), 500 (i), 800 (g), 1000 (k), 1500 μM (l), 1800 (m), and 2000 μM (n). **b** DPV peak currents of NO_2^- at 0.876 V versus NO_2^- concentration. The insert was the corresponding calibration curve. Results were expressed as the average of three independent experiments. Error bars represent standard deviations

activation energy (E_a) can be described according to the well-known Arrhenius equation [48]:

$$\ln k = \ln A - \frac{E_a}{RT} \tag{5}$$

Since the response peak current I is directly proportional to the rate constant k at fixed experimental conditions, the $\ln k$ can be replaced as $\ln I$ in the Arrhenius formula. The fitted regression equations are $\ln I_{pa}$ ($\ln \mu A$) = $-813.11/T$ (K^{-1}) + 5.08 with correlation coefficient of 0.9945 for bare GCE and $\ln I_{pa}$ ($\ln \mu A$) = $-744.76/T$ (K^{-1}) + 4.70 with correlation coefficient of 0.9978 for CG/PPy/CS/GCE. By linearly fitting the relationships between $\ln I$ and T^{-1}, it can be obtained that the E_a values for bare GCE and CG/PPy/CS/GCE are 6.19 and 6.76 kJ mol^{-1}, respectively. Therefore, the E_a value becomes higher on CG/PPy/CS/GCE. According to the theory of the

chemical kinetics, if the chemical reaction possesses higher E_a value, the reaction rate of this reaction will increase faster as the increase of the reaction temperature [49]. Above a certain temperature, the reaction rate of the reaction with higher E_a value can exceed that of the reaction having a smaller E_a. Herein, although the E_a value of CG/PPy/CS/GCE is larger, the reaction rates are much faster at all the measuring temperatures of NO_2^-. Thus, the electrochemical catalyst of CG/PPy/CS nanocomposite for the oxidation of NO_2^- is greatly enhanced to a certain extent.

Detection of nitrite

In order to get the maximum sensitivity for NO_2^- detection with CG/PPy/CS/GCE, the following parameters were optimized: (a) amount of CG, (b) amount ratio of Py to CG, (c) addition

Table 1 Comparison of the electrodes modified with CG/PPy/CS nanocomposite and other materials for the determination of NO_2^-

Electrode	Modifier	Technique	Linear range (μM)	Detection limit (μM)	Ref
Glassy carbon electrode	Carboxylated graphene oxide/lanthanum	Amperometry	1–750	0.07	27
Carbon paste electrode	Prussian blue	Amperometry	25–1000	9	31
Glassy carbon electrode	Liquid(1-(3-aminopropyl)-3-methylimidazolium bromide) and silicon carbide nanoparticles	Amperometry	0.05–0.35	0.019	7
Glassy carbon electrode	Fe_2O_3/reduced graphene oxide	Amperometry	0.05–780	0.015	33
Glassy carbon electrode	Fe_3O_4/reduced graphene oxide	Amperometry	1–92	0.3	34
Glassy carbon electrode	Graphene/hydroxyapatite	SWV	3–950	0.025	28
Platinum electrode	Zinc superoxide dismutase/nitrate reductase/carbon nanotubes/polypyrrole	CV	0.1–1000	0.05	32
Glassy carbon electrode	Graphene/poly-cyclodextrin/MWCNTs nanocomposite	DPV	5–750	1.65	15
Glassy carbon electrode	Pd nanoparticles/reduced graphene oxide	DPV	1–1000	0.23	8
Glassy carbon electrode	CG/PPy/CS	DPV	0.2–1000	0.02	This work

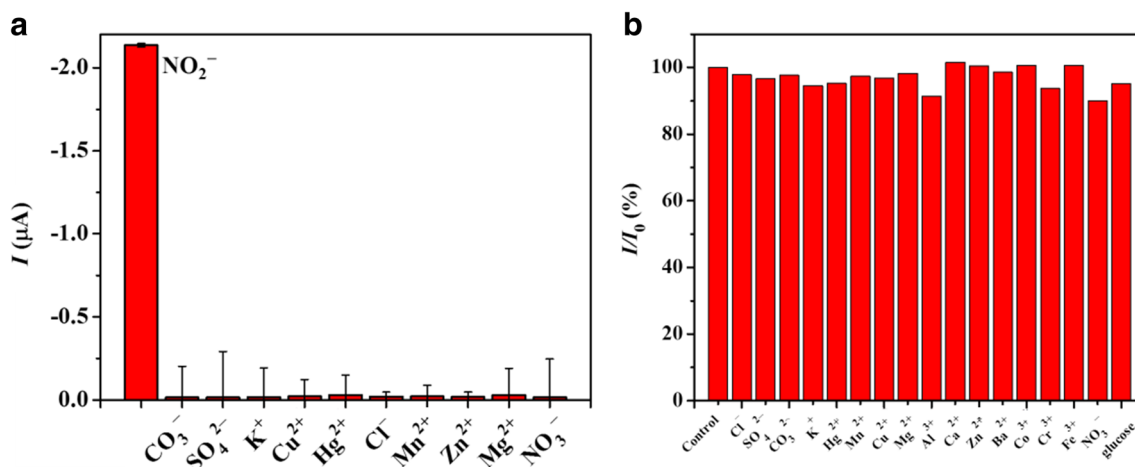*SWV* square wave voltammetry, *CV* cyclic voltammetry

Fig. 11 **a** DPV peak currents of CG/PPy/CS/GCE to different ions in 0.1 M NaAc–HAc buffer (pH 4.0). The concentration of NO_2^- is 10 μM. The concentrations of other ions are all 0.1 mM. **b** DPV peak currents of CG/PPy/CS/GCE to 10 μM NO_2^- in 0.1 M NaAc–HAc buffer (pH 4.0) with the addition of different ions. The concentrations of all ions are 1 mM. Results were expressed as the average of three independent experiments. Error bars represent standard deviations

volume, (d) buffer pH value. As shown in Fig. 9, the following experimental conditions are found to give the best results: (a) amount of CG of 4 mg mL^{-1}, (b) amount ratio of PPy to CG of 4:1, (c) addition volume of 4 μL, (d) buffer pH value of 4.0.

Table 2 Detection of NO_2^- in real water samples ($n = 5$)

Sample	Added (μM)	Found (μM)	Recovery (%)	R.S.D. (%)
Tap water	0	0	–	–
	5	4.81–5.15	96.2–103.0	2.4
	10	9.73–10.2	97.3–102.0	2.8
	20	19.6–19.9	98.0–99.5	1.7
	100	101.7–103.1	101.7–103.1	0.6
	200	190.8–197.3	95.4–98.7	1.6
	500	487.4–500.1	97.5–100.0	1.3
ONGFU SPRING water	0	0	–	–
	5	4.97–5.14	99.4–102.8	3.9
	10	9.7–10.3	97.0–103.0	2.6
	20	19.1–20.8	95.5–104.0	4.4
	100	95.9–102.4	95.9–102.4	4.4
	200	189.8–197.0	95.0–98.5	1.9
	500	494.6–505.7	98.9–101.1	1.1
Salt water	0	0	–	–
	5	4.9–5.2	98.0–104.0	2.5
	10	9.6–10.3	96.0–103.0	4.1
	20	19.3–20.8	96.5–104.0	3.3
	100	100.8–103.7	100.8–103.7	1.4
	200	201.9–207.6	101.0–103.8	1.5
	500	504.4–517.5	100.9–103.5	1.3
Soybean milk water	0	4.1–4.3	–	–
	5	9.1–9.4	100.0–104.5	2.8
	10	13.9–14.7	98.0–104.0	3.2
	20	23.9–24.9	99.0–103.0	1.4
	100	103.6–108.3	99.5–104.0	3.6
	200	203.4–211.4	99.7–103.6	2.7
	500	500.2–511.2	99.2–101.4	3.2

Under the optimum experimental conditions, DPV was employed for the determination of NO_2^- by utilizing CG/PPy/CS/GCE. Figure 10a displays the DPV responses of CG/PPy/CS/GCE for increasing the concentration of NO_2^- under the optimum experimental conditions. It is noticeable that the DPV peak currents at 0.876 V increase as the concentration of NO_2^- increases. As exhibited in Fig. 10b, a good relationship between the DPV peak currents and the NO_2^- concentration is further obtained. When the concentration of NO_2^- is in the range of 0.2 μM to 1000 μM, the DPV peak current is directly proportional to the concentration of NO_2^-. The linear regression equation for NO_2^- is I_{pa} (μA) $= -0.027$ c (μM) $+ 0.285$ with a correlation coefficient of 0.9991. Due to the high loading of CG/PPy/CS nanocomposite on GCE surface and the efficient electrochemical catalyst of CG/PPy/CS nanocomposite for the oxidation of NO_2^-, the detection limit of NO_2^- is estimated to be 0.02 μM according to the equation of $3\sigma/K$ (σ is the standard deviation of 11 measurements blank and K is the slope of calibration curve, respectively). Compared with some reported electrochemical methods (Table 1), our strategy has the comparable sensitivity and detection limit for NO_2^- detection with the simple electrode preparation procedure.

In addition, CG/PPy/CS/GCE shows good reproducibility for NO_2^- detection. The relative standard deviation (RSD) of same CG/PPy/CS/GCE response to 0.1 mM NO_2^- is 3.4% for 20 successive assays, and the RSD of five CG/PPy/CS/GCE responses to 0.1 mM NO_2^- is 1.2%. Additionally, the DPV peak current of same CG/PPy/CS/GCE is approximately 98.7 and 97.1% of its initial current response for 0.1 mM NO_2^- even after 10 and 18 days of storage, respectively. The excellent reproducibility and superior long-term stability of the constructed CG/PPy/CS/GCE is promising for NO_2^- anion determination.

Influences of other ions and real samples determination

To evaluate the selectivity of CG/PPy/CS/GCE for NO_2^- detection, the DPV responses of NO_2^- was examined in the presence of various environmentally relevant common anions (Cl^-, SO_4^{2-}, CO_3^{2-}, and NO_3^-) and metal ions (K^+, Cu^{2+}, Hg^{2+}, Mn^{2+}, Zn^{2+}, and Mg^{2+}) under the same conditions. The concentration of NO_2^- is 10 μM, while the concentrations of other ions are all 0.1 mM. As shown in Fig. 11a, significant increase of the DPV peak current is observed upon the addition of NO_2^-, while other common anions and metal ions exhibit a tiny variation of DPV peak current and such variation can be negligible, which indicates the high selectivity of CG/PPy/CS/GCE.

Furthermore, the interferences of common anions (Cl^-, SO_4^{2-}, CO_3^{2-}, and NO_3^-) and various metal ions (K^+, Hg^{2+}, Mn^{2+}, Cu^{2+}, Mg^{2+}, Al^{3+}, Ca^{2+}, Zn^{2+}, Ba^{2+}, Co^{3+}, Cr^{3+}, and Fe^{3+}) with concentrations of 1 mM on the determination of

10 μM NO_2^- were investigated at the optimal conditions. The DPV responses of NO_2^- at CG/PPy/CS/GCE are not affected by the presence of 100 times concentration of these anions and metal ions (Fig. 11b). Thus, this CG/PPy/CS/GCE shows excellent selectivity toward NO_2^- in the presence of common anions and metal ions.

To confirm the feasibility of the proposed method, this CG/PPy/CS/GCE was used to detect NO_2^- in water samples, including tap water, commercial NONGFU SPRING water, salt water, and soybean milk water. All these samples were filtered through a 0.22-μm membrane prior to detection. As indicated in Table 2, the DPV responses of NO_2^- in these water samples can be omitted, indicating that the concentrations of NO_2^- in these water samples are extremely low. Moreover, the recoveries of six different concentrations of NO_2^- range from 95.0 to 104.5% for five determinations, addressing the accuracy of this CG/PPy/CS/GCE for NO_2^- determination.

Conclusions

A novel and effective electrochemical sensing platform based on CG/PPy/CS/GCE for sensitive and highly selective detection of NO_2^- by DPV was developed. This method includes the polymerization of Py monomers on CG surface and the self-assemble of CG/PPy/CS nanocomposite on the surface of GCE. The synergistic effect of CG/PPy with high electron transfer ability and CS with abundant binding sites leads to the remarkably enhanced sensitivity and selectivity for NO_2^- detection. The prepared CG/PPy/CS/GCE exhibited excellent electrochemical properties such as wide linear range, low detection limit, good reproducibility, and high stability toward NO_2^-. The present electrochemical sensing platform can be applied for monitoring NO_2^- pollution.

References

1. Chen SF, Chen XQ, Xia TT, Ma Q (2016) A novel electrochemiluminescence sensor for the detection of nitroaniline based on the nitrogen-doped graphene quantum dots. Biosens Bioelectron 85:903–908

2. Mehmeti E, Stanković DM, Hajrizi A, Kalcher K (2016) The use of graphene nanoribbons as efficient electrochemical sensing material for nitrite determination. Talanta 159:34–39

3. Chen JH, Pang S, He LL, Nugen SR (2016) Highly sensitive and selective detection of nitrite ions using $Fe_3O_4@SiO_2$/Au magnetic

nanoparticles by surface-enhanced Raman spectroscopy. Biosens Bioelectron 85:726–733

4. Senra-Ferreiro S, Pena-Pereira F, Lavilla I, Bendicho C (2010) Griess micro-assay for the determination of nitrite by combining fibre optics-based cuvetteless UV–vis micro-spectrophotometry with liquid-phase microextraction. Anal Chim Acta 668:195–200

5. Kumar VV, Anthony SP (2014) Highly selective silver nanoparticles based label free colorimetric sensor for nitrite anions. Anal Chim Acta 842:57–62

6. Herrmann SS, Granby K, Duedahl-Olesen L (2015) Formation and mitigation of Nnitrosamines in nitrite preserved cooked sausages. Food Chem 174:516–526

7. Salimi A, Kurd M, Teymourian H, Hallaj R (2014) Highly sensitive electrocatalytic detection of nitrite based on SiC nanoparticles/ amine terminated ionic liquid modified glassy carbon electrode integrated with flow injection analysis. Sens Actuators B Chem 205:136–142

8. Li F, Yu SH, Thompson L, Yu AM (2015) Development of a novel nitrite electrochemical sensor by stepwise in situ formation of palladium and reduced graphene oxide nanocomposites. RSC Adv 5: 40111–40116

9. World Health Organization, guidelines for drinking water quality, 3rd ed. (incorporating 1st and 2nd addenda), Geneva, 2008

10. United States Environmental Protection Agency (2009) National Primary Drinking Water Regulations: contaminant specific fact sheets. Inorganic Chemicals, Consumer Version, Washington

11. Yang S, Wo Y, Meyerhoff ME (2014) Polymeric optical sensors for selective and sensitive nitrite detection using cobalt(III) corrole and rhodium(III) porphyrin as ionophores. Anal Chim Acta 843:89–96

12. Gu B, Huang LY, Hu JL, Liu JJ, Su W, Duan XL, Li HT, Yao SZ (2016) Highly selective and sensitive fluorescent probe for the detection of nitrite. Talanta 152:155–161

13. Khan MR, Wabaidur SM, Alothman ZA, Busquets R, Naushad M (2016) Method for the fast determination of bromate, nitrate and nitrite by ultra performance liquid chromatography-mass spectrometry and their monitoring in Saudi Arabian drinking water with chemometric data treatment. Talanta 152:513–520

14. Lin Z, Dou XN, Li HF, Ma Y, Lin JM (2015) Nitrite sensing based on the carbon dots-enhanced chemiluminescence from peroxynitrous acid and carbonate. Talanta 132:457–462

15. Zhang Y, Yuan R, Chai YQ, Li WJ, Zhong X, Zhong HA (2011) Simultaneous voltammetric determination for DA, AA and NO_2^- based on graphene/poly-cyclodextrin/MWCNTs nanocomposite platform. Biosens Bioelectron 26:3977–3980

16. Haldorai Y, Hwang SK, Gopalan AI, Huh YS, Han YK, Voit W, Sai-Anand G, Lee KP (2016) Direct electrochemistry of cytochrome c immobilized on titanium nitride/multi-walled carbon nanotube composite for amperometric nitrite biosensor. Biosens Bioelectron 79:543–552

17. Jiang JJ, Fan WJ, Du XZ (2014) Nitrite electrochemical biosensing based on coupled graphene and gold nanoparticles. Biosens Bioelectron 51:343–348

18. Rajesh S, Kanugula AK, Bhargava K, Ilavazhagan G, Kotamraju S, Karunakaran C (2010) Simultaneous electrochemical determination of superoxide anion radical and nitrite using Cu,ZnSOD immobilized on carbon nanotube in polypyrrole matrix. Biosens Bioelectron 26:689–695

19. Liu HB, Qiao L, Gan N, Lin SC, Cao YT, Hu FT, Wang JY, Chen YJ (2016) Electro-deposited poly-luminol molecularly imprinted polymer coating on carboxyl graphene for stir bar sorptive extraction of estrogens in milk. J Chromatogr B 1027:50–56

20. Li XJ, Guo QF, Cao W, Li YY, Du B, Wei Q (2014) Enhanced electrochemiluminescence from luminol at carboxyl graphene for detection of α-fetoprotein. Anal Biochem 457:59–64

21. Li D, Kaner RB (2008) Graphene-based materials. Science 320: 1170–1171

22. Liang B, Fang L, Yang G, Hu YC, Guo XS, Ye XS (2013) Direct electron transfer glucose biosensor based on glucose oxidase self-assembled on electrochemically reduced carboxyl graphene. Biosens Bioelectron 43:131–136

23. Huang KJ, Niu DJ, Sun JY, Han CH, Wu ZW, Li YL, Xiong XQ (2011) Novel electrochemical sensor based on functionalized graphene for simultaneous determination of adenine and guanine in DNA. Colloids Surf B Biointerfaces 82:543–549

24. Liu AR, Li C, Bai H, Shi GQ (2010) Electrochemical deposition of polypyrrole/sulfonated graphene composite films. J Phys Chem C 114:22783–22789

25. Ye DX, Luo LQ, Ding YP, Chen Q, Liu X (2011) A novel nitrite sensor based on graphene/polypyrrole/chitosan nanocomposite modified glassy carbon electrode. Analyst 136:4563–4569

26. Choi YS, Joo SH, Lee SA, You DJ, Kim H, Pak C, Chang H, Seung D (2006) Surface selective polymerization of polypyrrole on ordered mesoporous carbon: enhancing interfacial conductivity for direct methanol fuel cell application. Macromolecules 39:3275–3282

27. Ye FY, Feng CQ, Jiang JB, Han S (2015) Simultaneous determination of dopamine, uric acid and nitrite using carboxylated graphene oxide/lanthanum modified electrode. Electrochim Acta 182:935–945

28. Lavanya N, Sudhan N, Kanchana P, Radhakrishnan S, Sekar C (2015) A new strategy for simultaneous determination of 4-aminophenol, uric acid and nitrite based on a graphene/hydroxyapatite composite modified glassy carbon electrode. RSC Adv 5:52703–52709

29. Lee R, Tamm T, Temmer R, Aabloo A, Kiefer R (2013) Two formation mechanisms and renewable antioxidant properties of suspensible chitosan-PPy and chitosan-PPy-BTDA composites. Synth Met 164:6–11

30. Yang SL, Liu XY, Zeng XD, Xia BY, Gu JP, Luo SL, Mai NN, Wei WZ (2010) Farbication of nano-copper/carbon nanotubes/chitosan film by one-step electrodeposition and its sensitive determination of nitrite. Sens Actuators B Chem 145:762–768

31. Pradela-Filho LA, Oliveira BC, Takeuchi RM, Santos AL (2015) A Prussian blue-carbon paste electrode for selective cathodic amperometric determination of nitrite using a flow-injection analysis system with carrier recycling. Electrochim Acta 180:939–946

32. Madasamy T, Pandiaraj M, Balamurugan M, Bhargava K, Sethy NK, Karunakaran C (2014) Copper, zinc superoxide dismutase and nitrate reductase coimmobilized bienzymatic biosensor for the simultaneous determination of nitrite and nitrate. Biosens Bioelectron 52:209–215

33. Radhakrishnan S, Krishnamoorthy K, Sekar C, Wilson J, Kim SJ (2014) A highly sensitive electrochemical sensor for nitrite detection based on Fe_2O_3 nanoparticles decorated reduced graphene oxide nanosheets. Appl Catal B Environ 148−149:22–28

34. Teymourian H, Salimi A, Khezrian S (2013) Fe_3O_4 magnetic nanoparticles/reduced graphene oxide nanosheets as a novel electrochemical and bioeletrochemical sensing platform. Biosens Bioelectron 49:1–8

35. Huang S, Lu SY, Huang CS, Sheng JR, Su W, Zhang LX, Xiao Q (2015) Sensitive and selective stripping voltammetric determination of copper(II) using a glassy carbon electrode modified with amino-reduced graphene oxide and β–cyclodextrin. Microchim Acta 182: 2529–2539

36. Tang LH, Wang Y, Li YM, Feng HB, Lu J, Li JH (2009) Preparation, structure, and electrochemical properties of reduced graphene sheet films. Adv Funct Mater 19:2782–2789

37. Anson F (1964) Application of potentiostatic current integration to the study of the adsorption of cobalt(III)-(ethylenedinitrilo(tetraacetate) on mercury electrodes. Anal Chem 36:932–934

38. Nicholson RS (1965) Theory and application of cyclic voltammetry for measurement of electrode reaction kinetics. Anal Chem 37: 1351–1355
39. Bard AJ, Faulkner LR (2001) Electrochemical methods: fundamentals and applications, 2nd edn. John Wiley & Sons, New York
40. Velický M, Bradley DF, Cooper AJ, Hill EW, Kinloch IA, Mishchenko A, Novoselov KS, Patten HV, Toth PS, Valota AT, Worrall SD, Dryfe RAW (2014) Electron transfer kinetics on mono- and multilayer grapheme. ACS Nano 8:10089–10100
41. Park JH, Aluru NR (2010) Ordering-induced fast diffusion of nanoscale water film on graphene. J Phys Chem C 114:2595–2599
42. Huang S, Lu SY, Huang CS, Sheng JR, Zhang LX, Su W, Xiao Q (2016) An electrochemical biosensor based on single-stranded DNA modified gold electrode for acrylamide determination. Sens Actuators B Chem 224:22–30
43. Tang WW, Zhang M, Li WH, Zeng XP (2014) An electrochemical sensor based on polyaniline for monitoring hydroquinone and its damage on DNA. Talanta 127:262–268
44. Er E, Çelikkan H, Erk N, Aksu ML (2015) A new generation electrochemical sensor based on graphene nanosheets/gold nanoparticles/Nafion nanocomposite for determination of silodosin. Electrochim Acta 157:252–257
45. Laviron E (1974) Adsorption autoinhibition and autocatalysis in polarography and in linear potential sweep voltammetry. J Electroanal Chem Interfacial Electrochem 52:355–393
46. Bard AJ, Faulkner LR (2001) Electrochemical methods: fundamentals and applications, second edn. Wiley, New York
47. Heli H, Eskandari I, Sattarahmady N, Moosavi-Movahedi AA (2012) Cobalt nanoflowers: synthesis, characterization and derivatization to cobalt hexacyanoferrate—electrocatalytic oxidation and determination of sulfite and nitrite. Electrochim Acta 77:294–301
48. Sethuraman V, Muthuraja P, Anandha Raj J, Manisankar P (2016) A highly sensitive electrochemical biosensor for catechol using conducting polymer reduced grapheme oxide–metal oxide enzyme modified electrode. Biosens Bioelectron 84:112–119
49. Wang Y, Wang X, Li CM (2010) Electrocatalysis of Pd–Co supported on carbon black or ball-milled carbon nanotubes towards methanol oxidation in alkaline media. Appl Catal B 99:229–234